


RESEARCH ARTICLE | FEBRUARY 14 2025

Electronic structure of YV_6Sn_6 probed by de Haas–van Alphen oscillations and density functional theory

Special Collection: [Quantum Dynamics in Theory, Numerics and in Experimental Research](#)Kyryl Shtefiienko ; Cole Phillips; Shirin Mozaffari ; Richa P. Madhogaria; William R. Meier ; David G. Mandrus ; David E. Graf; Keshav Shrestha  

APL Quantum 2, 016118 (2025)
<https://doi.org/10.1063/5.0252563>



Articles You May Be Interested In

De Haas-van Alphen effect in the band antiferromagnet FeGe_2 : Development of spin splitting

Low Temp. Phys. (April 2014)

de Haas–van Alphen effect in the diborides ScB_2 , ZrB_2 , and HfB_2

Low Temp. Phys. (April 2007)

Anisotropic giant magnetoresistance and de Haas–van Alphen oscillations in layered topological semimetal crystals

AIP Advances (April 2022)



Special Topics Open for Submissions

[Learn More](#)

Electronic structure of YV_6Sn_6 probed by de Haas–van Alphen oscillations and density functional theory

Cite as: APL Quantum 2, 016118 (2025); doi: 10.1063/5.0252563

Submitted: 10 December 2024 • Accepted: 27 January 2025 •

Published Online: 14 February 2025



View Online



Export Citation



CrossMark

Kyryl Shtefiienko,¹ Cole Phillips,¹ Shirin Mozaffari,² Richa P. Madhogaria,² William R. Meier,² David G. Mandrus,^{2,3} David E. Graf,^{4,5} and Keshav Shrestha^{1,a)}

AFFILIATIONS

¹Department of Chemistry and Physics, West Texas A&M University, Canyon, Texas 79016, USA

²Department of Materials Sciences and Engineering, University of Tennessee, Knoxville, Tennessee 37996, USA

³Materials Science & Technology Division, Oak Ridge National Laboratory, Oak Ridge, TN 37831, USA

⁴Department of Physics, Florida State University, Tallahassee, Florida 32306, USA

⁵National High Magnetic Field Laboratory, Tallahassee, Florida 32310, USA

Note: This paper is part of the APL Quantum Special Topic on Quantum Dynamics in Theory, Numerics and in Experimental Research.

^{a)}Author to whom correspondence should be addressed: kshrestha@wtamu.edu or drkeshavshrestha@gmail.com

ABSTRACT

This study investigates the electronic structure of the vanadium-based kagome metal YV_6Sn_6 using magnetoresistance (MR) and torque magnetometry. The MR exhibits a nearly linear, non-saturating behavior, increasing by up to 55% at 35 T but shows no evidence of Shubnikov–de Haas oscillations. In contrast, the torque signal, measured up to 41.5 T, reveals clear de Haas–van Alphen (dHvA) oscillations over a wide frequency range, from a low frequency of $F_\alpha \sim 20$ T to high frequencies between 8 and 10 kT. Angular and temperature-dependent dHvA measurements were performed to probe the Fermi surface parameters of YV_6Sn_6 . The dHvA frequencies display weak angular dependence, and the effective mass, determined by fitting the temperature-dependent data to the Lifshitz–Kosevich formula, is $0.097 m_0$, where m_0 represents the free electron mass. To complement the experimental findings, we computed the electronic band structure and Fermi surface using density functional theory. The calculations reveal several notable features, including multiple Dirac points near the Fermi level, flatbands, and Van Hove singularities. Two bands cross the Fermi level, contributing to the Fermi surface, with theoretical frequencies matching well with the observed dHvA frequencies. These combined experimental and theoretical insights enhance our understanding of the electronic structure of YV_6Sn_6 and provide a valuable framework for studying other vanadium- and titanium-based kagome materials.

© 2025 Author(s). All article content, except where otherwise noted, is licensed under a Creative Commons Attribution (CC BY) license (<https://creativecommons.org/licenses/by/4.0/>). <https://doi.org/10.1063/5.0252563>

I. INTRODUCTION

Recently, kagome materials, with atomic arrangements resembling a corner-sharing kagome lattice, have attracted significant attention in condensed matter physics due to their fascinating properties, such as non-trivial topology, flatbands, charge-density wave (CDW), and superconductivity.^{1–3} A prototypical example is AV_3Sb_5 ($A = K, Rb, \text{ and } Cs$), also known as the “135” family, which forms a hexagonal lattice of V atoms coordinated by Sb atoms.^{4–6} AV_3Sb_5 exhibits superconductivity with T_c ranging from

$\sim 0.3\text{--}3$ K, CDW order near $T_{CDW} \sim 80\text{--}110$ K, and a Van Hove singularity, among other intriguing features.^{7–10} Electronic band structure calculations reveal several remarkable properties, including the presence of flatbands, Van Hove singularity points, Dirac points near the Fermi level, and non-trivial \mathbb{Z}_2 topological invariants. Recent quantum oscillation studies^{11–21} on AV_3Sb_5 have confirmed the non-trivial band topology and uncovered significant reconstruction of the Fermi surface in the CDW phase.

Another class of kagome compounds, RM_6X_6 , known as the 166 family, has been discovered, where R represents alkali,

alkaline earth, or rare earth metals (e.g., Li, Mg, Yb, Sm, Gd, etc.); M represents transition metals (e.g., Co, Cr, Mn, V, Ni, etc.); and X represents Si, Ge, or Sn.^{22–27} This family crystallizes in the MgFe_6Ge_6 prototype structure, exhibits significant chemical diversity, and, therefore, offers a wide range of functionalities. Several interesting physical phenomena have already been observed in this family, for example, a large anomalous Hall effect in LiMn_6Sn_6 , non-trivial topological properties in GdV_6Sn_6 ,^{24,28} Chern topological magnetism in TbMn_6Sn_6 ,² competing magnetic phases in YMn_6Sn_6 ,²⁹ and more. Notably, within this family, ScV_6Sn_6 is the only member to exhibit a CDW transition at $T_{\text{CDW}} = 92$ K.^{30,31} However, no superconductivity has been observed in ScV_6Sn_6 under either ambient conditions or high pressures up to 11 GPa.³² We recently reported on the electronic structure of ScV_6Sn_6 , studied using high-field torque measurements³³ and density functional theory (DFT), which probed its electronic bands and Fermi surface, uncovering its non-trivial topology.

This work focuses on YV_6Sn_6 , a member of the 166 kagome family. Figure 1(a) shows the unit cell (upper panel) and the kagome lattice (bottom panel) of vanadium atoms in YV_6Sn_6 . Previous electrical transport and magnetic studies by Pokharel *et al.*²² have shown that YV_6Sn_6 does not exhibit a magnetic transition or CDW order down to 2 K. Recent studies³⁴ suggest that the CDW phase in ScV_6Sn_6 originates from a structural instability caused by tin–tin bond modulation in the rare-earth–tin chains. This instability appears to be driven by the undersized scandium atoms, which allow the scandium–tin chains to rattle within the larger V–Sn framework. In contrast, yttrium is too large, preventing the rattling of the rare-earth–tin chain and inhibiting the development of a CDW phase in YV_6Sn_6 . DFT studies²² on this material have revealed a non-trivial band topology, confirmed by calculating the \mathbb{Z}_2 topological invariants. Here, we have investigated the electronic structure of YV_6Sn_6 by employing high-field torque measurements and DFT calculations. Torque measurements under applied fields of 41.5 T revealed well-defined de Haas–van Alphen (dHvA) oscillations with frequencies reaching up to 10 kT. DFT calculations of the electronic band structure show multiple Dirac points, Van Hove singularities, and flatbands near the Fermi level. A comparison of the theoretical frequencies derived from DFT with the experimental frequencies demonstrates good agreement.

II. EXPERIMENTAL AND COMPUTATIONAL DETAILS

High-quality single crystals of YV_6Sn_6 were synthesized via the tin flux method following the recipe in Refs. 34 and 35. Elemental Y (Alfa Aesar, 99.9%), V (Alfa Aesar, 99.8%), and Sn (Alfa Aesar, 99.9999%) were put in an alumina Canfield crucible set and then sealed in silica ampoules filled with about 0.2 atm argon. The ampoules were heated to 1150 °C over 12 h, held for 15 h, and cooled to 780 °C over 300 h. To remove the tin flux, the ampoules were centrifuged at 780 °C. To remove the remaining tin on the surface, the crystals were etched in an aqueous 10 wt. % HCl solution for 12–36 h. Temperature-dependent resistivity measurements were carried out in a physical property measurement system (Quantum Design) using the four-probe technique. Magnetoresistance (MR) and torque measurements with maximum applied magnetic fields up to 35 and 41.5 T, respectively, were carried out at the National High Magnetic Field Laboratory (NHMFL), Tallahassee, FL. Torque measurements were conducted using a miniature piezoresistive cantilever. A tiny single crystal of YV_6Sn_6 was selected and attached to the cantilever arm using vacuum grease and then mounted on a rotating platform of the measurement probe. The probe was slowly cooled down to a base temperature of 0.5 K. Two resistive elements on the cantilever were balanced at the base temperature before taking the field dependent and temperature dependent torque measurements. Magnetic fields were swept at each fixed temperature at a rate of 1.5 T/min.

Electronic structures were calculated using density functional theory (DFT) with the full-potential linearized augmented plane wave (FP-LAPW) method, as implemented in the WIEN2k code.³⁶ The exchange-correlation energies were treated using the standard generalized gradient approximation (PBE-GGA).³⁷ Internal atomic coordinates were optimized in the scalar relativistic mode until the forces on individual atoms were reduced to below 20 meV/Å. Spin–orbit coupling (SOC) was incorporated through the second variational step.³⁸ The energy convergence criterion for self-consistent calculations was set to 10^{-4} Ry. The atomic sphere radii (RMT) were chosen as 2.50 bohrs for Y, V, and Sn. Self-consistent calculations utilized a grid of 800 k -points across the full Brillouin zone, while a denser k -point mesh of 5000 points was employed for Fermi surface computations.

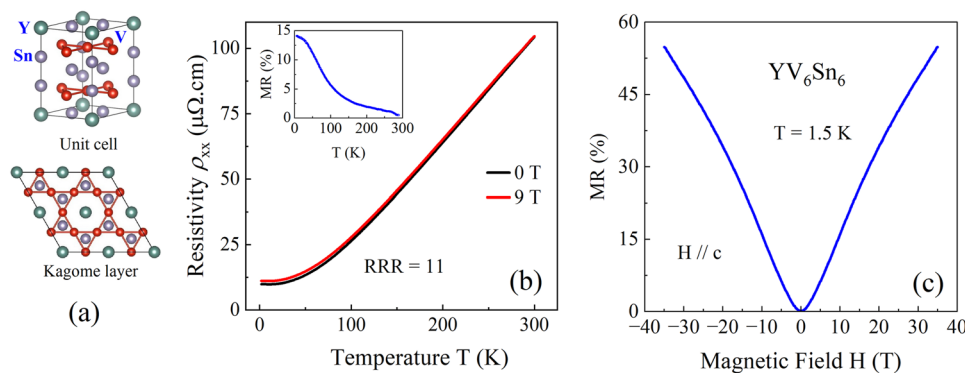


FIG. 1. (a) Unit cell (upper panel) and the top view (lower panel) of YV_6Sn_6 , illustrating the kagome network formed by V atoms. (b) Temperature dependence of resistivity for a YV_6Sn_6 single crystal at 0 and 9 T. Inset: Magnetoresistance (MR) vs temperature plot. (c) MR plot for a YV_6Sn_6 single crystal with the magnetic field applied along the c -axis at $T = 1.5$ K. The MR reaches up to 55%, with no sign of quantum oscillations.

III. RESULTS AND DISCUSSION

Figure 1(b) shows the electrical resistivity, ρ_{xx} , as a function of temperature. As seen in the graph, the resistivity decreases with temperature, indicating typical metallic behavior. The residual resistivity ratio (RRR), calculated by dividing ρ_{xx} at 300 K by its value at 2 K, is 11, indicating the high quality of our YV₆Sn₆ crystals. Upon applying a magnetic field of 9 T, the resistivity increases, as shown by the red curve. The $\rho_{xx}(T)$ exhibits a similar behavior to that observed in another 166 family member, LuV₆Sn₆.³⁵ The inset displays the magnetoresistance (MR), defined as $MR = [\rho_{xx}(9\text{ T}) - \rho_{xx}(0)]/\rho_{xx}(0)$, where $\rho_{xx}(9\text{ T})$ and $\rho_{xx}(0)$ represent the resistivity values at 9 and 0 T, respectively. As shown in the inset, the MR reaches as high as 15% at 2 K and decreases to nearly zero at 300 K. In order to understand the effect of a magnetic field on electrical transport, we measured the electrical resistance as a function of the magnetic field. Figure 1(c) shows the MR for YV₆Sn₆ with the magnetic field applied along the c-axis at $T = 1.5\text{ K}$. As seen in the graph, the MR increases nearly linearly with the applied field, without any indication of saturation. At 35 T, the MR reaches 55%, but no Shubnikov–de Haas oscillations are observed. However, observing quantum oscillations is essential to probe the Fermi surface of YV₆Sn₆. Therefore, we proceed with an alternative measurement technique: torque magnetometry.

Figure 2(a) shows the τ vs field plot at two different tilt angles, $\theta = -7^\circ$ and -21° . Here, θ is defined as the angle between the magnetic field and the c-axis of the sample, as depicted in the upper inset of Fig. 2(a). The dHvA oscillations are clearly observed at both angles above 5 T. In addition to the low-frequency signal, there is an additional high-frequency signal at high magnetic fields above 30 T. The high-frequency signal is more prominent at $\theta = -7^\circ$ compared to $\theta = -21^\circ$, as indicated by the dotted circle. This is clearer in the zoomed-in plot of the high-field region, shown in the lower inset. To extract the oscillation frequencies, we subtracted a smooth polynomial background from the torque data and then performed a fast Fourier transform (FFT). Figure 2(b) shows the Fourier transform of the torque data presented in Fig. 2(a). The low-frequency component, $F_\alpha = 25\text{ T}$, is present at both angles, as shown in the

inset. The torque signal at $\theta = -7^\circ$ exhibits additional frequencies at 180, 1400, and 8800 T. In contrast, at $\theta = -21^\circ$, these frequencies are completely overshadowed by the dominant lower frequency, F_α . Due to the low resolution of the high-frequency signal, it is difficult to extract from the torque data at some θ values. However, the lower frequency F_α is consistently observed at all measured angles. We observed a similar behavior in torque measurements³³ of another 166 compound, ScV₆Sn₆, where low frequencies are dominant and present at all θ values, while high frequencies are weak and only emerge at very high magnetic fields. This will be discussed in detail later.

In order to calculate the effective mass of charge carriers, we carried out the torque measurement at different temperatures. Figure 3(a) shows the temperature dependent torque data measured at $\theta = 28^\circ$. As seen in the graph, the dHvA oscillations are pronounced at low temperatures and gradually disappear at higher temperatures. At 35 K, the quantum oscillations are not visible. At this tilt angle, the lower frequency F_α changes to 18 T, and there is no interference from the high frequency signals, as seen in the frequency spectrum in Fig. 3(b). The amplitude of the frequency decreases at higher temperatures, and this behavior can be described by the Lifshitz–Kosevich (LK) theory.³⁹ According to the LK theory, the temperature dependent quantum oscillations in torque is given by

$$\Delta\tau(T, H) \propto e^{-\lambda_D} \frac{\lambda(T/H)}{\sin h[\lambda(T/H)]}, \quad (1)$$

with $\lambda_D(H) = \frac{2\pi^2 k_B}{\hbar e} m^* \frac{T_D}{H}$ and $\lambda(T/H) = \frac{2\pi^2 k_B}{\hbar e} m^* \frac{T}{H}$. Here, T_D , k_B , and m^* represent the Dingle temperature, Boltzmann’s constant, and effective mass of the charge carriers, respectively. The first term is the Dingle factor, which describes the attenuation of the oscillations with decreasing field H . The second term explains the weakening of the oscillations at higher temperatures.

The inset in Fig. 3(b) shows the FFT amplitude at different temperatures. The scattered squares represent the FFT amplitude,

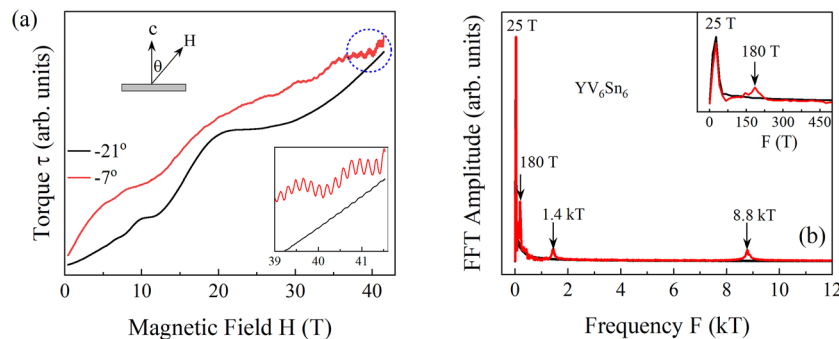


FIG. 2. (a) Torque (τ) of a YV₆Sn₆ single crystal measured up to 41.5 T at $\theta = -7^\circ$ and -21° and $T = 0.5\text{ K}$. The de Haas–van Alphen (dHvA) oscillations are observed at both angles above 5 T. A high-frequency signal is apparent at $\theta = -7^\circ$, as indicated by the dotted circle. Upper inset: A schematic diagram defining the tilt angle, θ . Lower inset: Zoomed-in torque data in the high-field region. The high-frequency signal is prominent at $\theta = -7^\circ$, although it is observed at both angles, -7° and -21° . (b) Frequency spectrum of the dHvA oscillations shown in (a). The low-frequency peak at $F_\alpha = 25\text{ T}$ is present at both angles, while three additional frequencies, 180, 1400, and 8800 T, are observed only at $\theta = -7^\circ$. Inset: A zoomed-in view of the frequency spectrum highlighting the lower frequencies.

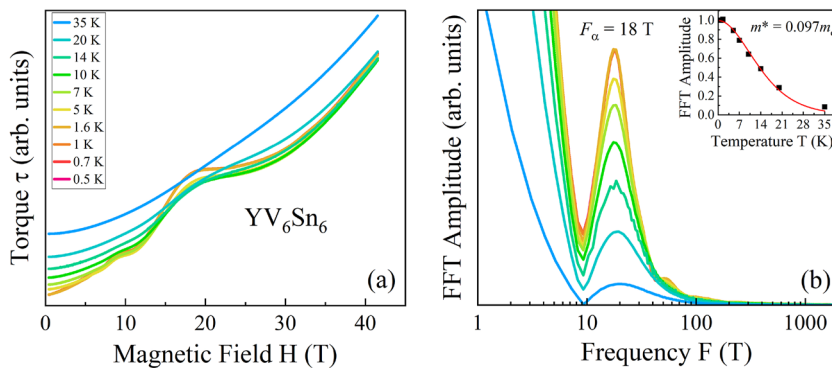


FIG. 3. Torque data of YV_6Sn_6 at different temperatures. The de Haas–van Alphen (dHvA) oscillations are visible at low temperatures and gradually diminish at higher temperatures. (b) Frequency spectrum of the torque data shown in (a). A prominent peak is observed at $F_\alpha = 18$ T in the frequency spectrum. Inset: temperature dependence of the frequency peak. The squares represent the data points, and the solid curve is the best fit using the Lifshitz–Kosevich formula.

while the solid red curve represents the best-fit curve to the data using the LK formula [Eq. (1)]. As shown in the graph, the LK formula explains the temperature-dependent behavior of the frequency. From the best fit, we determined $m^* = 0.097 m_0$, where m_0 is the rest mass of an electron. This m^* is comparable to the effective mass of other kagome systems^{40,43–45} reported previously.

The angular dependence of quantum oscillations provides information about the shape, size, and dimensionality of the Fermi surface.^{39,42–44} To explore this, we conducted torque measurements at various tilt angles. In Fig. 4(a), the torque data for YV_6Sn_6 measured at different θ values are shown. As shown in Fig. 4(a), there are clearly more than two periods, representing multiple quantum oscillation frequencies, and they seem to vary with θ values. Furthermore, the dHvA oscillations are present even if the magnetic field is perpendicular to the sample surface, indicating the three-dimensional nature of the Fermi surface. We have carried out background subtraction from the torque signal and determined the frequency values at different θ points, as presented in Fig. 4(b). For comparison purposes, we have also included possible theoretical frequencies computed by using DFT. We will discuss it in detail later.

From our high-field data, we observed a prominent peak at F_α , which appears to remain nearly constant while rotating the sample. In order to understand its topological feature, we calculated the

Berry phase (Φ_B) of the Fermi pocket of F_α using the Landau level (LL) fan plot, as shown in Fig. S1 of the [supplementary material](#). For a topologically non-trivial (or trivial) system, the Φ_B value is π (or zero).^{42,45} To avoid possible interference from other frequency signals, we employed the FFT bandpass filter approach^{21,40,46,47} to extract the oscillations corresponding to the particular frequency. When constructing this diagram, we assigned the LL index to the minima and maxima positions as $(N - \frac{1}{4})$ and $(N + \frac{1}{4})$, respectively.^{46–48} By performing a linear extrapolation of the data, represented by the dashed line, we derived an intercept $N_0 = 0.18 \pm 0.02$, corresponding to $\Phi_B = (0.36 \pm 0.04)\pi$. Although Φ_B is not exactly π , its non-zero value indicates the non-trivial topology of the α pocket. Furthermore, the slope value (18.1 ± 0.3) T closely matches the F_α value of 18 T in Fig. 3(b), validating the precision of the linear extrapolation in determining the intercept (and consequently the Φ_B value). Furthermore, the bandpass filter’s effectiveness in retaining the original dHvA oscillation signal without significant error is affirmed. A non-trivial Φ_B has been reported for the sister compound ScV_6Sn_6 using quantum oscillation studies.^{33,49}

To better understand the experimental observations, we computed the electronic band structure and Fermi surface of YV_6Sn_6 . Figure 5 illustrates the electronic band structures of YV_6Sn_6 (a) with-

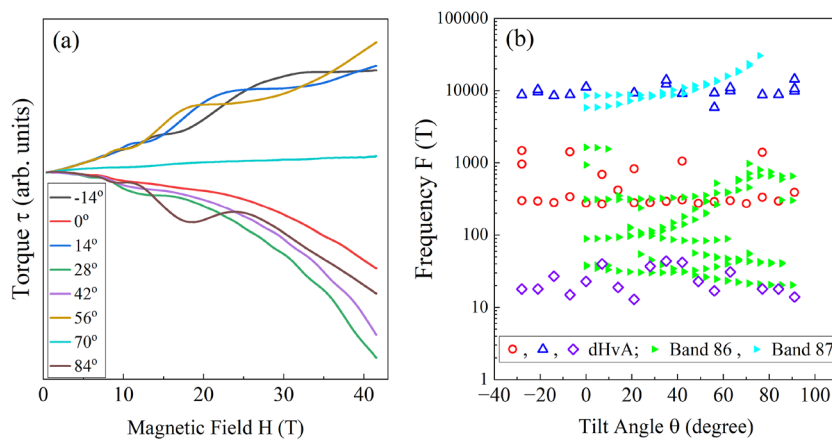


FIG. 4. (a) Angle-dependent torque signal for YV_6Sn_6 . The period, and thus the frequency, of quantum oscillations varies with the tilt angle θ . (b) Comparison of theoretical frequencies from **band 86** and **band 87** with experimental quantum oscillation frequencies. **Band 86** frequencies align well with experimental values below 1000 T, while higher frequencies, around 10 kT, correspond closely to those from **band 87**.

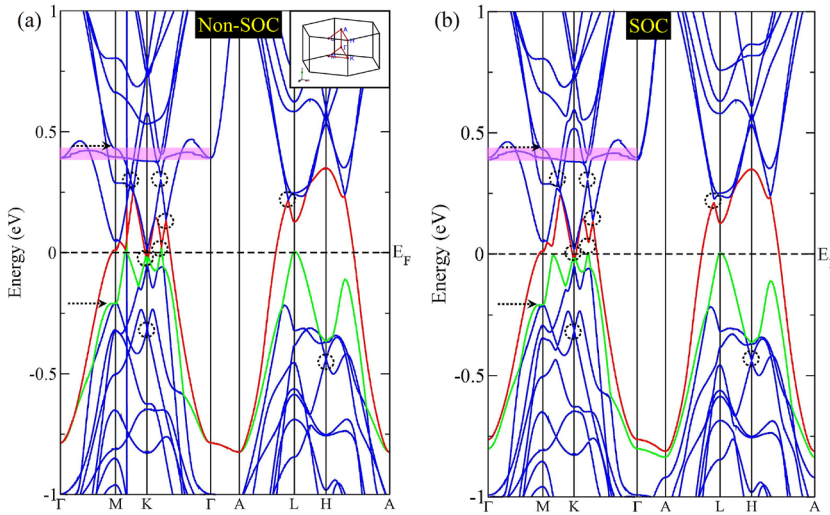


FIG. 5. Electronic band structure of pristine YV_6Sn_6 with (a) non-SOC and (b) SOC. The SOC is oriented along the [001] direction, corresponding to the out-of-plane axis of the material. The flat-band is denoted by the shaded purple area, and the Dirac points near the Fermi level are indicated by the dotted circles. Two bands, indicated by red and green colors, cross the Fermi level. The dashed arrows represent the Van Hove singularities. Inset: first Brillouin zone showing high-symmetry points.

out and (b) with the inclusion of spin-orbit coupling (SOC). The inset in Fig. 5(a) shows the high-symmetry points in the first Brillouin zone. As shown in Fig. 5(a), the electronic bands exhibit several intriguing features, including multiple Dirac points near the Fermi level (highlighted by the dotted circles), a flatband (shaded area), and multiple Van Hove singularities (indicated by the dashed arrows). Orbital-resolved electronic band structure provides detailed insights into the contributions of specific atomic orbitals to the electronic bands in a material. This information is critical for understanding the electronic, magnetic, and optical properties of materials. Therefore, we computed the orbital-resolved electronic bands of YV_6Sn_6 , as presented in Fig. S2 of the supplementary material. As shown in the graph, the electronic bands near the Fermi level are primarily dominated by the vanadium 3d orbitals. Moreover, features such as Dirac points, Van Hove singularities, and flatbands arise from the vanadium 3d and tin 5p orbitals. Notably, there appears to be no contribution from the yttrium 4d orbitals to the electronic bands of YV_6Sn_6 .

Here, we have aligned the SOC along the [001] direction, corresponding to the out-of-plane axis of the material. To investigate the magnetic anisotropy, we calculated the effect of SOC along various directions, including [001], [100], [110], and [111]. Our analysis revealed that [110] is the easy axis for magnetization, while [001] is the hard axis. By computing the total energy differences between magnetization orientations along different crystallographic directions, we determined the magnetic anisotropy energy to be 0.23 meV for YV_6Sn_6 .

Our electronic band structure is consistent with those calculated for other 166 kagome families.^{22,33,41,50,51} With the inclusion of SOC, the electronic bands slightly shift (either up or down), as shown in Fig. 5(b). Here, the SOC is oriented along the [001] direction, corresponding to the out-of-plane axis of the material. While some of the Dirac points develop gaps due to the inclusion of SOC, the flatbands and Van Hove singularity points remain nearly intact. For example, the previously gapless Dirac point along the K– Γ and A–L directions develops a gap as high as ~ 50 meV in the presence of SOC. There are two bands: **band 86** and **band 87** cross the Fermi

level, as indicated by the green and red colors, respectively. These bands contribute to the Fermi surface of YV_6Sn_6 .

Figure 6 shows the band-resolved Fermi surface of YV_6Sn_6 . The Fermi surface of **band 86** exhibits a chain-like feature at the Brillouin zone boundary, along with small pockets at the edge of the Brillouin zone. For **band 87**, there is a deformed, cylinder-like feature with a belly in the middle. The final inset represents the combined Fermi surface sheets from both bands. To understand the effect of SOC, we computed the Fermi surface of YV_6Sn_6 including the SOC effect, as shown in Fig. S3 of the supplementary material. It is found that the Fermi surface remains nearly unchanged. According to Onsager's relation,^{39,42,52,53} the frequency (F) of quantum oscillations is directly proportional to the cross-sectional area (A_F) of the Fermi surface as $F = \hbar/(2\pi e)A_F^2$, where \hbar is the reduced Planck constant and e is the charge of an electron. Therefore, we can calculate possible theoretical frequencies by measuring the cross-sectional area of the Fermi surface.

We employed the SKEAF code⁵⁴ for computing possible theoretical frequencies from the Fermi pockets derived from **band 86** and **band 87**. The calculated angular dependence of frequencies from different bands is plotted in Fig. 4(b) alongside the experimental data. As observed in the figure, frequencies derived from

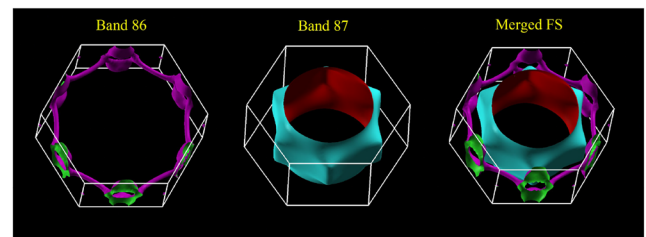


FIG. 6. Band-resolved Fermi surface (FS) of YV_6Sn_6 . Two bands: **band 86** and **band 87** contribute to the FS. The last inset is the combined FS sheets from both bands.

both **bands 86 and 87** describe the behavior of F_α . Low frequencies below 1000 T, observed in dHvA oscillations, are in good agreement with the theoretical frequencies computed from **band 86**. Similarly, the high-frequency signal near 10 kT is in good agreement with those computed from **band 87**. It is important to note that, although the frequency values are comparable, the angular dependence of the theoretical frequency derived from **band 87** shows an upward trend, especially above 60° , which is not clearly observed in the experimental data. The high frequency signal appears in very high fields (around 35 T) and is dominated by the low frequency signal, reducing its resolution [Figs. 4(a) and 2(a) and 2(b)]. This makes it challenging to track the angular dependence precisely. However, the angular dependence of the low frequencies is well captured by the frequencies derived from **band 86**. There are also possible frequencies below 100 T, but we did not observe these frequencies in our dHvA oscillation data. However, quantum oscillation experiments are not uncommon to miss higher frequencies.^{55,56}

IV. SUMMARY

Despite the chemical diversity of 166 compounds, there are limited studies^{33,41,49,50,57,58} that use quantum oscillations to understand their electronic properties. Moreover, most of these studies report the presence of low-frequency signals (below 100 T).^{49,57,58} For instance, Ma *et al.* performed Shubnikov–de Haas (SdH) oscillations in RMn_6Sn_6 ($R = \text{Gd–Tm, Lu}$) and observed frequencies below 100 T. This paper focuses on the detailed electrical transport, magnetotransport, and torque magnetometry studies of YV_6Sn_6 with applied fields up to 41.5 T. Our electrical transport measurement shows that this material demonstrates a good metallic behavior. To investigate the magnetotransport properties, we measured magnetoresistance (MR) with the applied fields up to 35 T. We found nearly a linearly varying and non-saturating MR with the value reaching as high as 55%; however, there is no clear sign of SdH oscillations in MR data. Therefore, we proceeded with another measurement technique: torque magnetometry. Our torque data, measured up to 41.5 T, show clear de Haas–van Alphen (dHvA) oscillations with the major frequency near 20 T, along with a high frequency signal as high as 10 kT.

To probe the Fermi surface properties, we performed both angular and temperature-dependent torque measurements. To complement the experimental results, we calculated the electronic band structure and the Fermi surface of YV_6Sn_6 using density functional theory (DFT). The calculations reveal several Dirac points near the Fermi level, along with notable features such as flatbands and Van Hove singularities. Two electronic bands cross the Fermi level, contributing to the Fermi surface. Unlike other kagome materials, the Fermi surface consists of a deformed cylindrical pocket at the center and chain-like features along the boundary of the Brillouin zone. By analyzing the cross-sectional areas of these Fermi pockets, we computed theoretical dHvA frequencies, which show good agreement with the experimentally observed values.

We did not observe SdH oscillations in YV_6Sn_6 even at a maximum applied magnetic field of 35 T [Fig. 1(c)]. This is likely due to the sensitivity of resistivity-based SdH measurements to various damping effects, including electron–phonon interactions and scattering from defects and impurities within the crystal, which can suppress quantum oscillations. In contrast, torque magnetometry,

which detects changes in magnetization, offers a higher signal-to-noise ratio and can amplify even subtle oscillations. Notably, torque measurements can resolve tiny high-frequency signals embedded within larger, low-frequency oscillations [Fig. 2(a)]. The proximity of multiple Dirac points near the Fermi level results in charge carriers behaving like massless Dirac fermions, characterized by exceptionally high mobility and unique quantum mechanical properties. As shown in Fig. 5, the flatband resides near the Fermi level (~ 0.4 eV above) and can be tuned closer through doping or application of external pressure. Furthermore, the presence of Van Hove singularities, or saddle points in the band structure where the density of states (DOS) diverges, significantly enhances electronic interactions, increasing the likelihood of emergent phenomena, such as magnetism, charge-density waves, and superconductivity. These combined experimental and computational insights presented here for YV_6Sn_6 provide a valuable foundation for understanding the electronic properties of other titanium- and vanadium-based kagome systems.

SUPPLEMENTARY MATERIAL

The [supplementary material](#) provides details on the Berry phase calculations (Fig. S1), orbital-resolved electronic band structures (Fig. S2), and band-resolved Fermi surfaces (Fig. S3) of YV_6Sn_6 .

ACKNOWLEDGMENTS

The work at West Texas A&M University (WTAMU) was supported by the Killgore Undergraduate and Graduate Student Research Grants, the Welch Foundation (Grant No. AE-0025), and the National Science Foundation (Award No. 2336011). DFT calculations were performed in the WTAMU HPC cluster, which was funded by the National Science Foundation (NSF CC* GROWTH 2018841). S.M. and D.G.M. acknowledge the support from AFOSR MURI (Grant No. FA9550-20-1-0322) and the support from the Gordon and Betty Moore Foundation (Grant No. GBMF9069). A portion of this work was performed at the National High Magnetic Field Laboratory, which is supported by National Science Foundation Cooperative Agreement No. DMR-2128556 and the State of Florida.

AUTHOR DECLARATIONS

Conflict of Interest

The authors have no conflicts to disclose.

Author Contributions

K.S. and C.P. contributed equally to this work.

Kyryl Shtefienko: Conceptualization (equal); Investigation (equal). **Cole Phillips:** Conceptualization (equal); Investigation (equal). **Shirin Mozaffari:** Conceptualization (equal); Investigation (equal). **Richa P. Madhogaria:** Conceptualization (equal); Investigation (equal). **William R. Meier:** Conceptualization (equal); Investigation

(equal). **David G. Mandrus**: Conceptualization (equal); Investigation (equal). **David E. Graf**: Conceptualization (equal); Investigation (equal). **Keshav Shrestha**: Conceptualization (lead); Formal analysis (equal); Investigation (lead); Writing – original draft (lead); Writing – review & editing (lead).

DATA AVAILABILITY

The data that support the findings of this study are available within the article.





REFERENCES

- ¹L. Ye, M. Kang, J. Liu, F. von Cube, C. R. Wicker, T. Suzuki, C. Jozwiak, A. Bostwick, E. Rotenberg, D. C. Bell, L. Fu, R. Comin, and J. G. Checkelsky, *Nature* **555**, 638 (2018).
- ²J.-X. Yin, W. Ma, T. A. Cochran, X. Xu, S. S. Zhang, H.-J. Tien, N. Shumiya, G. Cheng, K. Jiang, B. Lian et al., *Nature* **583**, 533 (2020).
- ³K. Jiang, T. Wu, J.-X. Yin, Z. Wang, M. Z. Hasan, S. D. Wilson, X. Chen, and J. Hu, *Natl. Sci. Rev.* **10**, nwac199 (2022).
- ⁴B. R. Ortiz, L. C. Gomes, J. R. Morey, M. Winiarski, M. Bordelon, J. S. Mangum, I. W. H. Oswald, J. A. Rodriguez-Rivera, J. R. Neilson, S. D. Wilson, E. Ertekin, T. M. McQueen, and E. S. Toberer, *Phys. Rev. Mater.* **3**, 094407 (2019).
- ⁵B. R. Ortiz, P. M. Sarte, E. M. Kenney, M. J. Graf, S. M. L. Teicher, R. Seshadri, and S. D. Wilson, *Phys. Rev. Mater.* **5**, 034801 (2021).
- ⁶B. R. Ortiz, S. M. Teicher, Y. Hu, J. L. Zuo, P. M. Sarte, E. C. Schueller, A. M. Abeykoon, M. J. Krogstad, S. Rosenkranz, R. Osborn, R. Seshadri, L. Balents, J. He, and S. D. Wilson, *Phys. Rev. Lett.* **125**, 247002 (2020).
- ⁷F. H. Yu, D. H. Ma, W. Z. Zhuo, S. Q. Liu, X. K. Wen, B. Lei, J. J. Ying, and X. H. Chen, *Nat. Commun.* **12**, 3645 (2021).
- ⁸K. Y. Chen, N. N. Wang, Q. W. Yin, Y. H. Gu, K. Jiang, Z. J. Tu, C. S. Gong, Y. Uwatoko, J. P. Sun, H. C. Lei, J. P. Hu, and J. Cheng, *Phys. Rev. Lett.* **126**, 247001 (2021).
- ⁹N. N. Wang, K. Y. Chen, Q. W. Yin, Y. N. N. Ma, B. Y. Pan, X. Yang, X. Y. Ji, S. L. Wu, P. F. Shan, S. X. Xu, Z. J. Tu, C. S. Gong, G. T. Liu, G. Li, Y. Uwatoko, X. L. Dong, H. C. Lei, J. P. Sun, and J.-G. Cheng, *Phys. Rev. Res.* **3**, 043018 (2021).
- ¹⁰M. Kang, S. Fang, J.-K. Kim, B. R. Ortiz, S. H. Ryu, J. Kim, J. Yoo, G. Sangiovanni, D. D. Sante, B.-G. Park, C. Jozwiak, A. Bostwick, E. Rotenberg, E. Kaxiras, S. D. Wilson, J.-H. Park, and R. Comin, *Nat. Phys.* **18**, 301 (2022).
- ¹¹F. H. Yu, T. Wu, Z. Y. Wang, B. Lei, W. Z. Zhuo, J. J. Ying, and X. H. Chen, *Phys. Rev. B* **104**, 041103 (2021).
- ¹²Q. Yin, Z. Tu, C. Gong, Y. Fu, S. Yan, and H. Lei, *Chin. Phys. Lett.* **38**, 037403 (2021).
- ¹³S.-Y. Yang, Y. Wang, B. R. Ortiz, D. Liu, J. Gayles, E. Derunova, R. Gonzalez-Hernandez, L. Šmejkal, Y. Chen, S. S. P. Parkin, S. D. Wilson, E. S. Toberer, T. McQueen, and M. N. Ali, *Sci. Adv.* **6**, eabb6003 (2020).
- ¹⁴K. Nakayama, L. Yongkai, T. Kato, M. Liu, Z. Wang, T. Takahashi, Y. Yao, and T. Sato, *Phys. Rev. X* **12**, 011001 (2022).
- ¹⁵B. R. Ortiz, S. M. L. Teicher, L. K. abd Paul, M. Sarte, J. P. C. Ruff, R. Seshadri, and S. D. Wilson, *Phys. Rev. X* **11**, 041030 (2021).
- ¹⁶H. Luo, Q. Gao, H. Liu, Y. Gu, D. Wu, C. Yi, J. Jia, S. Wu, X. Luo, Y. Xu et al., *Nat. Commun.* **13**, 273 (2022).
- ¹⁷Y. Fu, N. Zhao, Z. Chen, Q. Yin, Z. Tu, C. Gong, C. Xi, X. Zhu, Y. Sun, K. Liu, and H. Lei, *Phys. Rev. Lett.* **127**, 207002 (2021).
- ¹⁸W. Zhang, L. Wang, C. W. Tsang, X. Liu, J. Xie, W. C. Yu, K. T. Lai, and S. K. Goh, *Phys. Rev. B* **106**, 195103 (2022).
- ¹⁹C. Broyles, D. Graf, H. Yang, X. Dong, H. Gao, and S. Ran, *Phys. Rev. Lett.* **129**, 157001 (2022).
- ²⁰K. Shrestha, M. Shi, T. Nguyen, D. Miertschin, K. Fan, L. Deng, D. E. Graf, X. Chen, and C.-W. Chu, *Phys. Rev. B* **107**, 075120 (2023).
- ²¹K. Shrestha, R. Chapai, B. K. Pokharel, D. Miertschin, T. Nguyen, X. Zhou, D. Y. Chung, M. G. Kanatzidis, J. F. Mitchell, U. Welp, D. Popović, D. E. Graf, B. Lorenz, and W. K. Kwok, *Phys. Rev. B* **105**, 024508 (2022).
- ²²G. Pokharel, S. M. L. Teicher, B. R. Ortiz, P. M. Sarte, G. Wu, S. Peng, J. He, R. Seshadri, and S. D. Wilson, *Phys. Rev. B* **104**, 235139 (2021).
- ²³J. Lee and E. Mun, *Phys. Rev. Mater.* **6**, 083401 (2022).
- ²⁴S. Peng, Y. Han, G. Pokharel, J. Shen, Z. Li, M. Hashimoto, D. Lu, B. R. Ortiz, Y. Luo, H. Li, M. Guo, B. Wang, S. Cui, Z. Sun, Z. Qiao, S. D. Wilson, and J. He, *Phys. Rev. Lett.* **127**, 266401 (2021).
- ²⁵E. Rosenberg, J. M. DeStefano, Y. Guo, J. S. Oh, M. Hashimoto, D. Lu, R. J. Birgeneau, Y. Lee, L. Ke, M. Yi, and J.-H. Chu, *Phys. Rev. B* **106**, 115139 (2022).
- ²⁶X. Zhang, Z. Liu, Q. Cui, Q. Guo, N. Wang, L. Shi, H. Zhang, W. Wang, X. Dong, J. Sun, Z. Dun, and J. Cheng, *Phys. Rev. Mater.* **6**, 105001 (2022).
- ²⁷G. Pokharel, B. Ortiz, J. Chamorro, P. Sarte, L. Kautzsch, G. Wu, J. Ruff, and S. D. Wilson, *Phys. Rev. Mater.* **6**, 104202 (2022).
- ²⁸Y. Hu, X. Wu, Y. Yang, S. Gao, N. C. Plumb, A. P. Schnyder, W. Xie, J. Ma, and M. Shi, *Sci. Adv.* **8**, eadd2024 (2022).
- ²⁹N. J. Ghimire, R. L. Dally, L. Poudel, D. Jones, D. Michel, N. T. Magar, M. Bleuel, M. A. McGuire, J. Jiang, J. Mitchell et al., *Sci. Adv.* **6**, eabe2680 (2020).
- ³⁰H. W. S. Arachchige, W. R. Meier, M. Marshall, T. Matsuoka, R. Xue, M. A. McGuire, R. P. Hermann, H. Cao, and D. Mandrus, *Phys. Rev. Lett.* **129**, 216402 (2022).
- ³¹T. Hu, H. Pi, S. Xu, L. Yue, Q. Wu, Q. Liu, S. Zhang, R. Li, X. Zhou, J. Yuan, D. Wu, T. Dong, H. Weng, and N. Wang, *Phys. Rev. B* **107**, 165119 (2023).
- ³²X. Zhang, J. Hou, W. Xia, Z. Xu, P. Yang, A. Wang, Z. Liu, J. Shen, H. Zhang, X. Dong, Y. Uwatoko, J. Sun, B. Wang, Y. Guo, and J. Cheng, *Materials* **15**, 7372 (2022).
- ³³K. Shrestha, B. Regmi, G. Pokharel, S.-G. Kim, S. D. Wilson, D. E. Graf, B. A. Magar, C. Phillips, and T. Nguyen, *Phys. Rev. B* **108**, 245119 (2023).
- ³⁴W. R. Meier, R. P. Madhugaria, S. Mozaffari, M. Marshall, D. E. Graf, M. A. McGuire, H. W. S. Arachchige, C. L. Allen, J. Driver, H. Cao, and D. Mandrus, *J. Am. Chem. Soc.* **145**, 20943 (2023).
- ³⁵S. Mozaffari, W. R. Meier, R. P. Madhugaria, N. Peshcherenko, S.-H. Kang, J. W. Villanova, H. W. S. Arachchige, G. Zheng, Y. Zhu, K.-W. Chen, K. Jenkins, D. Zhang, A. Chan, L. Li, M. Yoon, Y. Zhang, and D. G. Mandrus, *Phys. Rev. B* **110**, 035135 (2024).
- ³⁶P. Blaha, K. Schwarz, G. K. Madsen, D. Kvasnicka, and J. Luitz, *An Augmented Plane Wave Plus Local Orbitals Program for Calculating Crystal Properties* (Schwarz, Vienna University of Technology, Austria, 2001), Vol. 60.
- ³⁷J. P. Perdew, K. Burke, and M. Ernzerhof, *Phys. Rev. Lett.* **77**, 3865 (1996).
- ³⁸K. Koepernik and H. Eschrig, *Phys. Rev. B* **59**, 1743 (1999).
- ³⁹D. Shoenberg, *Magnetic Oscillations in Metals* (Cambridge University Press, 1984).
- ⁴⁰C. Phillips, K. Shtefienko, T. Nguyen, A. N. Capa Salinas, B. A. Magar, G. Pokharel, S. D. Wilson, D. E. Graf, and K. Shrestha, *Phys. Rev. B* **110**, 205135 (2024).
- ⁴¹C. Dhital, G. Pokharel, B. Wilson, I. Kendrick, M. M. Asmar, D. Graf, J. Guerrero-Sanchez, R. Gonzalez-Hernandez, and S. D. Wilson, *Phys. Rev. B* **109**, 235145 (2024).
- ⁴²B. R. Ortiz, P. M. Sarte, E. M. Kenney, M. J. Graf, S. M. L. Teicher, R. Seshadri, and S. D. Wilson, *Phys. Rev. Mater.* **5**, 034801 (2021).
- ⁴³K. Shrestha, V. Marinova, D. Graf, B. Lorenz, and C. W. Chu, *Phys. Rev. B* **95**, 075102 (2017).
- ⁴⁴K. Shrestha, D. Graf, V. Marinova, B. Lorenz, and C. W. Chu, *J. Appl. Phys.* **122**, 125901 (2017).
- ⁴⁵K. Shrestha, “Magnetotransport studies on topological insulators,” Doctoral dissertation, University of Houston (2015), see <https://hdl.handle.net/10657/4881>.
- ⁴⁶T. Nguyen, N. Aryal, B. K. Pokharel, L. Harnagea, D. Miertschin, D. Popović, D. E. Graf, and K. Shrestha, *Phys. Rev. B* **106**, 075154 (2022).
- ⁴⁷K. Shrestha, M. Shi, B. Regmi, T. Nguyen, D. Miertschin, K. Fan, L. Z. Deng, N. Aryal, S.-G. Kim, D. E. Graf, X. Chen, and C. W. Chu, *Phys. Rev. B* **107**, 155128 (2023).
- ⁴⁸K. Shrestha, D. Miertschin, R. Sankar, B. Lorenz, and C. W. Chu, *J. Phys.: Condens. Matter* **33**, 335501 (2021).

- ⁴⁹G. Zheng, Y. Zhu, S. Mozaffari, N. Mao, K.-W. Chen, K. Jenkins, D. Zhang, A. Chan, H. W. S. Arachchige, R. P. Madhogaria *et al.*, *J. Phys.: Condens. Matter* **36**, 215501 (2024).
- ⁵⁰E. Rosenberg, J. M. DeStefano, Y. Lee, C. Hu, Y. Shi, D. Graf, S. M. Benjamin, L. Ke, and J.-H. Chu, *Phys. Rev. B* **110**, 035119 (2024).
- ⁵¹S. R. Bhandari, M. Zeeshan, V. Gusain, K. Shrestha, and D. Rai, *APL Quantum* **1**, 046118 (2024).
- ⁵²K. Shrestha, V. Marinova, B. Lorenz, and P. C. W. Chu, *Phys. Rev. B* **90**, 241111 (2014).
- ⁵³K. Shrestha, V. Marinova, B. Lorenz, and C. W. Chu, *J. Phys.: Condens. Matter* **30**, 185601 (2018).
- ⁵⁴P. Rourke and S. Julian, *Comput. Phys. Commun.* **183**, 324 (2012).
- ⁵⁵W. Zheng, R. Schönemann, S. Mozaffari, Y.-C. Chiu, Z. B. Goraum, N. Aryal, E. Manousakis, T. M. Siegrist, K. Wei, and L. Balicas, *Phys. Rev. B* **102**, 125103 (2020).
- ⁵⁶D. Rhodes, R. Schönemann, N. Aryal, Q. Zhou, Q. R. Zhang, E. Kampert, Y.-C. Chiu, Y. Lai, Y. Shimura, G. T. McCandless, J. Y. Chan, D. W. Paley, J. Lee, A. D. Finke, J. P. C. Ruff, S. Das, E. Manousakis, and L. Balicas, *Phys. Rev. B* **96**, 165134 (2017).
- ⁵⁷W. Ma, X. Xu, J.-X. Yin, H. Yang, H. Zhou, Z.-J. Cheng, Y. Huang, Z. Qu, F. Wang, M. Z. Hasan, and S. Jia, *Phys. Rev. Lett.* **126**, 246602 (2021).
- ⁵⁸M. He, X. Xu, D. Li, Q. Zeng, Y. Liu, H. Zhao, S. Zhou, J. Zhou, and Z. Qu, *Phys. Rev. B* **109**, 155117 (2024).

RESEARCH ARTICLE | DECEMBER 10 2024

Electron beam-splitting effect with crossed zigzag graphene nanoribbons in high-spin metallic states

Special Collection: [Quantum Dynamics in Theory, Numerics and in Experimental Research](#)Sofia Sanz ; Géza Giedke ; Daniel Sánchez-Portal ; Thomas Frederiksen  Check for updates

APL Quantum 1, 046122 (2024)

<https://doi.org/10.1063/5.0233722>View
OnlineExport
Citation

Articles You May Be Interested In

Edge and substrate-induced bandgap in zigzag graphene nanoribbons on the hexagonal nitride boron 8-ZGNR/h-BN(0001)

AIP Advances (September 2013)

First-principles study of the transport behavior of zigzag graphene nanoribbons tailored by strain

AIP Advances (January 2012)

Enhancement of thermospin effect in ZGNRs via p - n co-doping on edge

J. Appl. Phys. (October 2016)



Special Topics Open for Submissions

[Learn More](#)

Electron beam-splitting effect with crossed zigzag graphene nanoribbons in high-spin metallic states

Cite as: APL Quantum 1, 046122 (2024); doi: 10.1063/5.0233722

Submitted: 16 August 2024 • Accepted: 13 November 2024 •

Published Online: 10 December 2024



View Online



Export Citation



CrossMark

Sofia Sanz,^{1,2,a)}  Géza Giedke,^{1,3}  Daniel Sánchez-Portal,²  and Thomas Frederiksen^{1,3} 

AFFILIATIONS

¹ Donostia International Physics Center (DIPC), E-20018 Donostia-San Sebastián, Spain

² Centro de Física de Materiales (CFM) CSIC-UPV/EHU, E-20018 Donostia-San Sebastián, Spain

³ IKERBASQUE, Basque Foundation for Science, E-48013 Bilbao, Spain

Note: This paper is part of the APL Quantum Special Topic on Quantum Dynamics in Theory, Numerics and in Experimental Research.

^{a)} Author to whom correspondence should be addressed: sofia.sanzwuhl@ehu.eus

ABSTRACT

Here, we analyze the electron transport properties of a device formed of two crossed graphene nanoribbons with zigzag edges (ZGNRs) in a spin state with total magnetization different from zero. While the ground state of ZGNRs has been shown to display antiferromagnetic ordering between the electrons at the edges, for wide ZGNRs—where the localized spin states at the edges are decoupled and the exchange interaction is close to zero—in the presence of relatively small magnetic fields, the ferromagnetic (FM) spin configuration can become the state of lowest energy due to the Zeeman effect. In these terms, by comparing the total energy of a periodic ZGNR as a function of the magnetization per unit cell, we obtain the FM-like solution of the lowest energy for the perfect ribbon, the corresponding FM-like configuration of the lowest energy for the four-terminal device formed of crossed ZGNRs, and the critical magnetic field needed to excite the system to this spin configuration. By performing transport calculations, we analyze the role of the distance between layers and the crossing angle of this device in the electrical conductance, at small gate voltages. The problem is approached employing the mean-field Hubbard Hamiltonian in combination with non-equilibrium Green's functions. We find that ZGNR devices subject to transverse magnetic fields may acquire a high-spin configuration that ensures a metallic response and tunable beam-splitting properties, making this setting promising for studying electron quantum optics with single-electron excitations.

© 2024 Author(s). All article content, except where otherwise noted, is licensed under a Creative Commons Attribution (CC BY) license (<https://creativecommons.org/licenses/by/4.0/>). <https://doi.org/10.1063/5.0233722>

I. INTRODUCTION

The increasing interest in graphene nanoribbons (GNRs) for molecular-scale electronic and spintronic devices has emerged because it is well known that they inherit some of the exceptional properties of graphene while having tunable electronic properties, such as the dependence of the bandgap on their width and edge topology,¹ and the appearance of π -magnetism,² absent in pure two-dimensional (2D) graphene. Moreover, these systems are a remarkable platform for electron quantum optics, where the electrons propagating coherently in these ballistic conductors resemble

photons propagating in optical waveguides.³ On the one hand, it has been shown that electrons can propagate without scattering over large distances of the order of ~ 100 nm in GNRs.^{4–6} On the other hand, ballistic transport in ZGNRs can be fairly unsusceptible to edge defects as a consequence of the prevailing Dirac-like behavior, which makes the electronic current flow maximally through the central region of the ribbon.⁷ Furthermore, with the advent of bottom-up fabrication techniques, long samples of GNRs free of defects can now be chemically realized via on-surface synthesis, as demonstrated in the seminal works by Cai *et al.* for armchair GNRs⁸ and by Ruffieux *et al.* for ZGNRs.⁹

It is known that the ground state of ZGNRs corresponds to a ferromagnetic (FM) ordering of spins along the edges and antiferromagnetic (AFM) ordering between the edges,^{10,11} i.e., with total spin projection per unit cell equal to zero, $S_z = 0$. In this configuration, the magnetic instabilities of the states localized at the edges coming from the flat bands of ZGNRs open a bandgap due to the Coulomb repulsion in the otherwise metallic ribbons.¹² The opening of the bandgap and the edge states associated with the AFM coupling in ZGNRs have been confirmed by experiments, where the magnetic order has been shown to be stable up to room temperature.^{13,14} The spin-polarized states localized at the edges are coupled such that there is an energy penalty to excite the AFM ground state to the FM state (exchange interaction). In the case of wider ZGNRs, the AFM and FM solutions are close in energy (small exchange interaction) due to the decoupling of the localized edge states, as they decay exponentially toward the center of the ribbon.^{10,15–18} In this case, the FM solution can be favored due to the Zeeman energy under a relatively small magnetic field. The presence of a net spin-polarization, in the absence of transition metals or heavy atoms, makes these structures privileged for spintronics due to the weak spin scattering in pure carbon-based systems.^{2,19} For instance, the intrinsically weak spin-orbit and hyperfine couplings in graphene lead to long spin coherence and relaxation times²⁰ and a large spin-diffusion length that is expected to reach $\sim 10 \mu\text{m}$ even at room temperature.²¹

Recently, devices formed of crossed GNRs have been predicted to behave as perfect beam splitters, where the injected electron beam is divided into two of the four arms with near 50–50 probability and zero backscattering.^{22–24} Furthermore, the particular case of devices formed of crossed ZGNRs is even more interesting, since they can create a spin-polarizing scattering potential²⁵ where the device can work as a spin-polarizing beam splitter. Following these ideas for electron quantum optics applications, a Mach–Zehnder-like interferometer in a GNRs network has recently been proposed.²⁶ In terms of their feasibility, manipulation of GNRs in STMs^{27,28} has opened the possibility of building 2D multi-terminal GNR-based electronic circuits.²⁹ The spin properties of such devices can be addressed by measuring with spin-polarized STMs^{30,31} and probed by shot-noise measurements.³² For instance, a device formed of two crossed ZGNRs has been experimentally realized with the control over the crossing angle reaching a precision of 5° .³³

While, in previous studies, only the AFM regime has been explored, other spin configurations can appear and show interesting spin-polarized transport properties. For instance, in contrast to the AFM case, the FM band structure of periodic ZGNRs does not show a bandgap around the Fermi level, which makes this regime interesting since there is conduction of electrons at the Fermi level. Given the metallic character of the FM-like spin configuration, one can envision to generate a minimal excitation in the device with only one particle and no hole (a leviton)^{34–37} by applying a Lorentzian-like voltage pulse of specific amplitude and duration, enabling the generation of a single-electron excitation.³⁸

Here, we analyze the functioning of an electronic beam splitter built with two crossed ZGNRs (of width 30 carbon atoms across) in an FM-like configuration, i.e., where the total magnetization of the device is different from zero. To describe the spin physics of the system, we employ the Hubbard Hamiltonian in the mean-field approximation (MFH).³⁹ The main complexity of the modeling lies in the description of the coupling between ZGNRs at the crossing,

for which we use a Slater–Koster parameterization⁴⁰ that has shown to be in good agreement with other more accurate descriptions, such as density functional theory.²⁴ By employing this simple, yet powerful description based on single-electron physics, we can explore large systems composed of ~ 8000 atoms.

The manuscript is structured as follows: In Sec. II, we explain in detail the theoretical methods employed in this work (MFH Hamiltonian and NEGF formalism). In Sec. III, we present the obtained results for a device formed of two crossed-wide ZGNRs in its FM-like configuration, and finally, the conclusions are provided in Sec. IV.

II. METHODS

The system of study is composed of two infinite crossed ZGNRs placed one on top of the other separated by an inter-ribbon distance d , with a relative crossing angle of around $\theta = 60^\circ$, as shown in Fig. 1. Here, the semi-infinite electrodes are indicated by red squares numbered 1–4.

To describe the π -electrons, responsible for the spin polarization and the transport phenomena in the system in the presence of Coulomb repulsion, we employ the MFH Hamiltonian³⁹ with a single p_z orbital per site,

$$H_{\text{MFH}} = \sum_{ij,\sigma} t_{ij} c_{i\sigma}^\dagger c_{j\sigma} + U \sum_{i,\sigma} n_{i\sigma} \langle n_{i\bar{\sigma}} \rangle. \quad (1)$$

Here, $c_{i\sigma}$ ($c_{i\sigma}^\dagger$) is the annihilation (creation) operator of an electron at site i with spin $\sigma = \{\uparrow, \downarrow\}$ and $n_{i\sigma} = c_{i\sigma}^\dagger c_{i\sigma}$ is the corresponding number operator. The tight-binding parameters t_{ij} are described by Slater–Koster two-center σ - and π -type integrals between two p_z

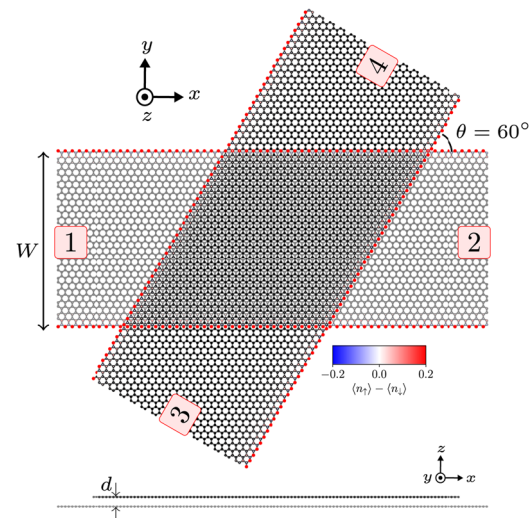


FIG. 1. Top and side views of the device geometry with spin density distribution. The size of the blobs is proportional to the magnitude of the spin polarization, $\langle n_\uparrow \rangle - \langle n_\downarrow \rangle$, and the color depicts the sign of the spin polarization as indicated by the color bar placed as an inset figure. The four numbered electrodes are indicated in red squares. The crossing angle between the ribbons in this geometry is $\theta = 60^\circ$. The layers are separated by a distance d . The width (W) of the ribbons is 30 atoms across.

atomic orbitals⁴⁰ as used previously for twisted-bilayer graphene⁴¹ and crossed GNRs.^{24–26} U accounts for the Coulomb interaction between two electrons occupying the same p_z orbital. The total Hamiltonian H_T is the composition of the device Hamiltonian H_D , the electrodes Hamiltonian for the periodic leads H_α , and the coupling between these two $H_{\alpha D}$, i.e., $H_T = H_D + \sum_\alpha (H_\alpha + H_{\alpha D})$. More details for the implementation can be found in Refs. 25, 26, and 42.

As the junction between the ribbons breaks the translational invariance of the perfect ZGNRs, we use Green's function^{43,44} formalism to solve the Schrödinger equation for the open quantum system. Details of the implemented MFH model with open boundary conditions⁴² can be found in the supplementary material of Ref. 25.

The transport properties are analyzed by computing the transmission probabilities per spin index $\sigma = \{\uparrow, \downarrow\}$, between the different pairs of terminals as a function of the electron energy E from the Landauer–Büttiker formula,^{45,46}

$$T_{\alpha\beta}^\sigma(E) = \text{Tr} \left[\Gamma_\alpha^\sigma \mathbf{G}^\sigma \Gamma_\beta^\sigma \mathbf{G}^{\sigma\dagger} \right], \quad (2)$$

where \mathbf{G} is the retarded Green's function and Γ_α is the broadening matrix of lead α , due to the coupling of the device to this lead. See Ref. 26 for further details on the implementation. From the transmission probability, one can obtain the zero-bias conductance, calculated as

$$G_{\alpha\beta}^\sigma = G_0 \sum_n T_{\alpha\beta}^{\sigma n}(E_F), \quad (3)$$

where G_0 is the conductance quantum and $T_{\alpha\beta}^{\sigma n}(E_F)$ is the transmission of the n th available channel at the Fermi level E_F , which is related to Eq. (2) by $T_{\alpha\beta}^\sigma(E) = \sum_n T_{\alpha\beta}^{\sigma n}(E)$. Note that, around E_F , there is only one single transverse mode (channel) available, and therefore, $T_{\alpha\beta}^{\sigma n}(E) = T_{\alpha\beta}^\sigma(E)$. To compute the transmission probabilities, we use the open-source code TBTRANS⁴⁷ and the Python package SISL for post-processing.⁴⁸

III. RESULTS

In this section, we analyze the transport properties for a device formed of two crossed ZGNRs of $W = 30$ carbon atoms across (30-ZGNR) as a function of the inter-layer separation d for values close to the typical distance between layers in graphite ($d = 3.34$ Å), and the intersecting angle θ for values close to the commensurate case where $\theta = 60^\circ$. To understand the spin states of ZGNRs, we performed different spin-polarized calculations changing the total mean value of the spin operator \hat{S}_z per unit cell, $\langle \hat{S}_z \rangle = \frac{1}{2} \sum_i (\langle n_{i\uparrow} \rangle - \langle n_{i\downarrow} \rangle) \equiv S_z$, where the summation goes over the sites i within the unit cell of the periodic ZGNR.

In Fig. 2(a), we show the total energy per unit cell as a function of S_z relative to the case of $S_z = 0$ (the AFM case) for a periodic ZGNR of $W = 30$ carbons across. As can be seen here, there is a local minimum at $S_z = 0.317$, corresponding to the solution of the lowest energy for $S_z \neq 0$. The fact that the solution of minimum energy appears at such total S_z can be understood from the fact that, in the AFM case, the local spin projection summed over the bottom (or top) half of the unit cell of the ZGNR is $|S_z^{\text{half}}| = 0.159$. This means that the total S_z per unit cell in the FM case needs to reach twice this value to flip the local magnetic moment at one edge. Note that

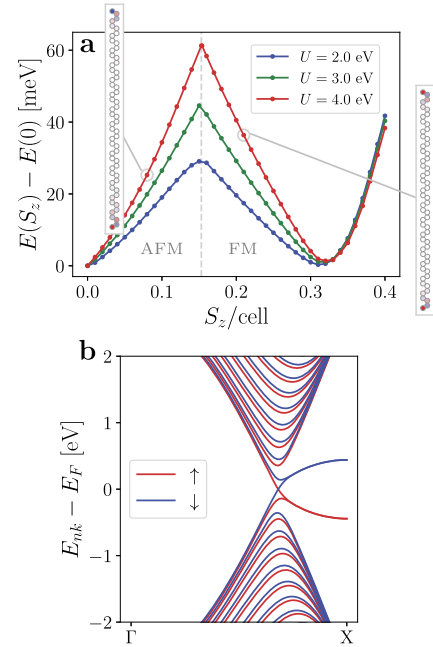


FIG. 2. (a) Energy differences between MFH solutions calculated with $U = 2$ eV (blue line), $U = 3$ eV (green line), and $U = 4$ eV (red line), obtained by imposing different spin projections S_z per unit cell. The dashed line separates the two phases depending on S_z (AFM and FM). The inset figures show examples of the spin polarization for the AFM and FM configurations, calculated with $S_z = 0.08$ and $S_z = 0.21$, respectively, where the red color indicates the up-spin majority, while the blue color indicates the down-spin majority. (b) Band structure of the periodic 30-ZGNR calculated with $U = 3.0$ eV for $S_z = 0.317$. Red and blue lines represent the up- and down-spin components, respectively.

the magnetic moment associated with S_z is $\mu = g_S \mu_B S_z$, where $g_S \approx 2$ is the electron spin g -factor and μ_B is the Bohr magneton. To see to what extent the ribbon width affects these results, we compare $E(S_z)$ for $W = 10, 20, 30, 40$ -ZGNRs in Fig. S1 in the [supplementary material](#), where we observe two main features: While the qualitative behavior is the same for all of them, the value of S_z at which the minimum of energy appears is larger for wider ribbons, and, as expected, the minimum value of $E(S_z > 0)$ diminishes with the width.

For each S_z , we plot the energy corresponding to the spin configuration of the lowest energy in Fig. 2(a). Here, we distinguish between two phases depending on S_z : AFM character (for $S_z < 0.15$), where the spin polarization shows opposite spin majorities at the edges, and FM character (for $S_z > 0.15$), where the spin polarization shows the spin majority of equal spin index. The two insets to Fig. 2(a) show the spin polarization for a 30-ZGNR: one in the AFM-like spin configuration (calculated with $S_z = 0.08$), where it can be seen that the colors at the edges are different (red and blue), and another one in the FM-like spin configuration (calculated with $S_z = 0.21$), where it can be seen that the same color appears at both edges (red). In the case of the AFM-like spin configuration for $S_z \neq 0$, not only the sign of the local magnetic moments at the bottom and top edges of the unit cell is different but also the magnitude, as a consequence of the existing spin imbalance. Whereas when the FM character is achieved, both the magnitude and sign of the local

magnetic moments at the bottom and top edges of the unit cell are equal.

In Fig. 2(b), we plot the band structure for the FM solution of the lowest energy for the 30-ZGNR, obtained with $S_z = 0.317$, for spin $\sigma = \uparrow$ (red lines) and $\sigma = \downarrow$ (blue lines). Here, we can observe the metallic character of the FM configuration for the ZGNR, as there are states available at the Fermi level, E_F , for both up and down spins.

As mentioned above, although the ground state corresponds to the configuration with $S_z = 0$, the presence of a magnetic field B in the z -direction (cf. Fig. 1) can stabilize a high-spin configuration due to the Zeeman energy $\Delta E = \mu B = g_s \mu_B S_z B$. For instance, the corresponding electronic energy $E(S_z)$ for the FM-like configuration of the lowest energy is $E(S_z = 0.317) = 0.97$ meV/cell above the ground state, implying that a critical magnetic field of the order $B_c = 26.6$ T (parallel to the z -axis in this case) is needed to make the two spin states degenerate. In Fig. 3(a), we study the zero-bias conductance $G_{\alpha\beta}(V)$ with $(\alpha, \beta) \in \{(1, 2), (1, 3)\}$ (black and green lines, respectively) for a device formed of two crossed 30-ZGNRs as a function of the inter-layer separation d . Here, V represents a rigid shift of the Fermi level E_F . We consider inter-layer distances close to the typical van der Waals distance between graphene layers in graphite ($d = 3.34$ Å).^{23,49,50} In the first place, we can infer that the total spin-averaged conductance (sum of intra- and inter-layer conductances) is 1 since the values for \bar{G}_{12} and \bar{G}_{13} are symmetric with respect to $0.5G_0$, which means that there is no backscattering for an incoming electron at the Fermi level in these devices at least for these ranges of d and θ . In the second place, we observe an oscillating behavior of $\bar{G}_{\alpha\beta}$ with respect to this varying parameter. For instance, the inter-/intra-layer conductance ratio reaches its maximum for $d = 3.34$ Å. While one would expect that for smaller inter-layer distances d the interlayer (\bar{G}_{13}) conductance would increase, as the interlayer hopping integral depends exponentially on the distance between the ribbons, we observe a decrease (and increase in \bar{G}_{12}) for smaller d in Fig. 3(a), as a consequence of an interference process due to the scattering potential created by the crossing. We also observe that, for d between 3.44 and 3.49 Å, there is a crossing between \bar{G}_{12} and \bar{G}_{13} , implying that, for that inter-layer separation, the device behaves as a perfect 50:50 beam splitter where the incoming electron beam is equally separated in the two possible outgoing directions with $\bar{G}_{\alpha\beta} = 0.5G_0$ for low gate voltages V .

Similarly, in Fig. 3(b), we study $G_{\alpha\beta}(V)$ for different crossing angles close to the commensurate configuration with $\theta = 60^\circ$. We apply the rotation around the center of the scattering region (crossing) that is obtained for the case with $\theta = 60^\circ$ and accounts for the effect of different possible stackings by averaging over the in-plane translations of one ribbon with respect to the other. By doing so, we aim to provide a comprehensive overview of the results, accounting for the variability in stacking configurations that might occur in practical scenarios. The in-plane unit cell is determined by the graphene lattice vectors. We obtain the conductance for a mesh of four points along each lattice vector within the unit cell. The error bars are calculated as the standard deviation of the spin-averaged conductance $\bar{G}_{\alpha\beta}$ at each point, averaging over the in-plane translations. The observed variance of approximately $\sim 10\%$ – 20% reflects the variations across different translational configurations, showing the inherent differences sampled by these translations. However, not all the stackings are equivalent. For instance, the most energetically favorable (and therefore most likely) configuration is the

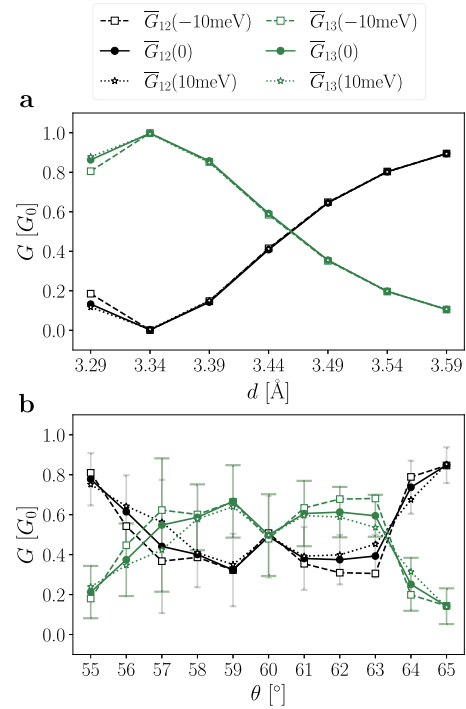


FIG. 3. Spin-averaged conductance $\bar{G}_{\alpha\beta}(V)$ between incoming electrode $\alpha = 1$ and outgoing electrodes $\beta = 2$ (black lines) and $\beta = 3$ (green lines) in units of the conductance quantum G_0 , as a function of (a) the inter-layer separation d , with fixed crossing angle $\theta = 60^\circ$ and stacking as shown in Fig. 1, and (b) the crossing angle θ averaged over the in-plane translations of one ribbon with respect to the other, with fixed $d = 3.34$ Å, for a device formed of crossed 30-ZGNRs obtained with $U = 3.0$ eV in the FM configuration. The error bars in (b) are calculated as the standard deviation of $\bar{G}_{\alpha\beta}(0)$ at each θ by averaging over the different displacements. We obtain this conductance at different gate voltages $V = -10$ meV (dashed lines with open squares), $V = 0$ (solid lines with filled circles), and $V = 10$ meV (dotted lines with open stars). The legend placed on top is common to both panels (a) and (b).

AB-stacking (see the supplementary material of Ref. 25). By analyzing the transport properties relative to this varying parameter in Fig. 3(b), we observe, on the one hand, that the inter-/intra-layer conductance ratio reaches its maximum for $\theta = 55^\circ, 65^\circ$. On the other hand, the sum of the total spin-averaged conductance is 1 as in panel (a), since the values for \bar{G}_{12} and \bar{G}_{13} are symmetric with respect to $0.5G_0$ as well, meaning that the variation of θ does not introduce backscattering. We can see that the oscillatory dependence of the conductance on the crossing angle is less smooth than the one seen in Fig. 3(a). This occurs due to a more complicated dependence of the σ - and π -type hopping integrals on θ .

To see the effect of the width on the transport properties as a function of these two varying parameters, we performed a similar analysis for a 20-ZGNR device in the [supplementary material](#) (see Fig. S2), where we observe that, qualitatively, the behavior is maintained. For further detail, we plot the energy-resolved transmission probabilities for the 30-ZGNR device as a function of d and θ in the [supplementary material](#) (see Figs. S3 and S4).

Finally, we note that it has been previously shown that the symmetries associated with the spatial distribution of the spin densities are crucial for the transport properties of the device.^{24,25} In this case, since the FM character implies that $\langle n_{\uparrow} \rangle \neq \langle n_{\downarrow} \rangle$, there will not be a symmetric behavior for the existing spin channels. However, the spin-density distribution possesses a symmetry axis at $y = \sin(-60^\circ)x$ that maps the device geometry to itself through mirror operations, and applies to each spin component individually (conserves the spin index). As it has been shown in Refs. 24 and 25, certain symmetrical combinations of electrodes lead to equal transmission probabilities $T_{\alpha\beta}^{\sigma} = T_{\gamma\delta}^{\sigma}$. In this case, the symmetrical electrode mapping corresponds to $(1, 2, 3, 4) \leftrightarrow (4, 3, 2, 1)$.

IV. CONCLUSIONS

We have analyzed the electron transport properties for a device formed of two crossed infinite ZGNRs of $W = 30$ carbon atoms across (30-ZGNRs) as a function of the spin configuration by fixing different values for the total spin per unit cell S_z . In the first place, by computing the total energy associated with these configurations $E(S_z)$, we have shown that there is a local minimum for the solution with $S_z > 0$, with $E(S_z > 0)$ close to 1 meV/cell above the ground state $[E(0)]$. We have also seen that, depending on S_z , there are two possible phases: AFM-character, where the edges of the ZGNR unit cell are populated by opposite spin majorities, and FM-character, where the two edges of the ribbon are populated by the same spin majority. These two phases appear for $S_z < 0.15$ and $S_z > 0.15$, respectively. We also computed the band structure for the FM-like configuration of the lowest energy, where we observe that this system in such a spin state shows a metallic character. We estimate that the critical magnetic field needed to make this FM-like solution degenerate with the AFM ground state is $B_c = 26.6$ T for this particular case, although this value will further decrease for wider ribbons.

We have also calculated the inter- and intra-layer electrical conductances for different gatings varying the inter-layer distances, for distances close to the van der Waals distance between graphene layers in graphite ($d = 3.34$ Å), and crossing angles close to the commensurate stacking where $\theta = 60^\circ$ for this four-terminal device. We have shown that the (spin- and displacement-averaged) electrical conductance displays an oscillatory behavior with respect to these varying parameters at low gate voltages ($-10 \text{ meV} \leq V \leq 10 \text{ meV}$) while maintaining the sum $\bar{G}_{12} + \bar{G}_{13} = 1$, which means that there is no backscattering for the devices for different values of d and θ within the shown ranges nor conductance into terminal 4. The maximum value for the inter-/intra-layer spin-averaged conductance ratio ($\bar{G}_{13}/\bar{G}_{12}$) for this device is found for $d = 3.34$ Å and $\theta = 55^\circ, 65^\circ$. In addition, to show that these results are not exclusive to the chosen ZGNR width, we performed a similar analysis for a 20-ZGNR device (see [supplementary material](#)), where we show that it possesses similar qualitative behavior.

The results presented here add to the vision of using GNR-based devices for spintronics and quantum technologies. On top of the already discussed properties and applications of spin-polarized GNR-based beam splitters for electron quantum optics,^{24–26} this device in its FM-like spin configuration can be a promising candidate due to its metallic nature, which facilitates electron injection through the generation of a minimal excitation. This can be achieved

by applying a Lorentzian-like voltage pulse with a specific amplitude and duration to produce a single-electron excitation within the device.^{34–37} In fact, performing time-dependent quantum transport calculations for levitonic excitations^{34–37} could offer critical insights into the nonequilibrium dynamics of the proposed devices, and further elucidate the role of minimal excitation states in transport phenomena of the charges injected by the pulse.^{51–53}

SUPPLEMENTARY MATERIAL

See the [supplementary material](#) for additional calculations, including transport calculations for devices with other ribbon widths and transmission curves as a function of electronic energy for the device discussed in the main text.

ACKNOWLEDGMENTS

This work was funded by the Spanish Grant No. MCIN/AEI/10.13039/501100011033 (Grant Nos. PID2020-115406GB-I00, TED2021-132388B-C44, PID2022-140845OB-C66, and JDC2022-048665-I), the Basque Department of Education (Grant No. PIBA-2023-1-0021), the University of the Basque Country (UPV/EHU) through Grant No. IT-1569-22, and the European Union's Horizon 2020 (FET-Open project SPRING Grant No. 863098).

AUTHOR DECLARATIONS

Conflict of Interest

The authors have no conflicts to disclose.

Author Contributions

Sofia Sanz: Conceptualization (equal); Data curation (equal); Formal analysis (equal); Funding acquisition (equal); Investigation (equal); Software (equal); Visualization (equal); Writing – original draft (equal); Writing – review & editing (equal). **Géza Giedke:** Formal analysis (supporting); Funding acquisition (equal); Investigation (equal); Supervision (supporting); Writing – original draft (supporting); Writing – review & editing (equal). **Daniel Sánchez-Portal:** Formal analysis (supporting); Funding acquisition (equal); Investigation (equal); Supervision (supporting); Writing – original draft (supporting); Writing – review & editing (equal). **Thomas Frederiksen:** Data curation (supporting); Formal analysis (equal); Funding acquisition (lead); Investigation (equal); Resources (equal); Software (equal); Supervision (equal); Visualization (equal); Writing – original draft (supporting); Writing – review & editing (equal).

DATA AVAILABILITY

The dataset that supports the findings of this study is publicly available on Zenodo, <https://doi.org/10.5281/zenodo.14224593>.

REFERENCES

- Y.-W. Son, M. L. Cohen, and S. G. Louie, “Half-metallic graphene nanoribbons,” *Nature* **444**, 347 (2006).

- ²D. G. de Oteyza and T. Frederiksen, “Carbon-based nanostructures as a versatile platform for tunable π -magnetism,” *J. Phys.: Condens. Matter* **34**, 443001 (2022).
- ³H. Chakraborti, C. Gorini, A. Knothe, M.-H. Liu, P. Makk, F. D. Parmentier, D. Perconte, K. Richter, P. Rouleau, B. Sacépé, C. Schönberger, and W. Yang, “Electron wave and quantum optics in graphene,” *J. Phys.: Condens. Matter* **36**, 393001 (2024).
- ⁴S. Minke, J. Bundesmann, D. Weiss, and J. Eroms, “Phase coherent transport in graphene nanoribbons and graphene nanoribbon arrays,” *Phys. Rev. B* **86**, 155403 (2012).
- ⁵J. Baringhaus, M. Ruan, F. Edler, A. Tejada, M. Sicut, A. Taleb-Ibrahimi, A.-P. Li, Z. Jiang, E. H. Conrad, C. Berger, C. Tegenkamp, and W. A. de Heer, “Exceptional ballistic transport in epitaxial graphene nanoribbons,” *Nature* **506**, 349 (2014).
- ⁶J. Aprojanz, S. R. Power, P. Bampoulis, S. Roche, A.-P. Jauho, H. J. W. Zandvliet, A. A. Zakharov, and C. Tegenkamp, “Ballistic tracks in graphene nanoribbons,” *Nat. Commun.* **9**, 4426 (2018).
- ⁷L. P. Zárbo and B. K. Nikolić, “Spatial distribution of local currents of massless Dirac fermions in quantum transport through graphene nanoribbons,” *Europhys. Lett.* **80**, 47001 (2007).
- ⁸J. Cai, P. Ruffieux, R. Jaafar, M. Bieri, T. Braun, S. Blankenburg, M. Muoth, A. P. Seitsonen, M. Saleh, X. Feng, K. Müllen, and R. Fasel, “Atomically precise bottom-up fabrication of graphene nanoribbons,” *Nature* **466**, 470 (2010).
- ⁹P. Ruffieux, S. Wang, B. Yang, C. Sánchez-Sánchez, J. Liu, T. Dienel, L. Talirz, P. Shinde, C. A. Pignedoli, D. Passerone, T. Dumslaff, X. Feng, K. Müllen, and R. Fasel, “On-surface synthesis of graphene nanoribbons with zigzag edge topology,” *Nature* **531**, 489 (2016).
- ¹⁰M. Fujita, K. Wakabayashi, K. Nakada, and K. Kusakabe, “Peculiar localized state at zigzag graphite edge,” *J. Phys. Soc. Jpn.* **65**, 1920 (1996).
- ¹¹H. Lee, Y.-W. Son, N. Park, S. Han, and J. Yu, “Magnetic ordering at the edges of graphitic fragments: Magnetic tail interactions between the edge-localized states,” *Phys. Rev. B* **72**, 174431 (2005).
- ¹²Y.-W. Son, M. L. Cohen, and S. G. Louie, “Energy gaps in graphene nanoribbons,” *Phys. Rev. Lett.* **97**, 216803 (2006).
- ¹³G. Z. Magda, X. Jin, I. Hagymási, P. Vancsó, Z. Osváth, P. Nemes-Incze, C. Hwang, L. P. Biró, and L. Tapasztó, “Room-temperature magnetic order on zigzag edges of narrow graphene nanoribbons,” *Nature* **514**, 608–611 (2014).
- ¹⁴Y. Y. Li, M. X. Chen, M. Weinert, and L. Li, “Direct experimental determination of onset of electron-electron interactions in gap opening of zigzag graphene nanoribbons,” *Nat. Commun.* **5**, 4311 (2014).
- ¹⁵K. Nakada, M. Fujita, G. Dresselhaus, and M. S. Dresselhaus, “Edge state in graphene ribbons: Nanometer size effect and edge shape dependence,” *Phys. Rev. B* **54**, 17954 (1996).
- ¹⁶K. Wakabayashi, M. Fujita, H. Ajiki, and M. Sigríst, “Electronic and magnetic properties of nanographite ribbons,” *Phys. Rev. B* **59**, 8271 (1999).
- ¹⁷Y. Miyamoto, K. Nakada, and M. Fujita, “First-principles study of edge states of H-terminated graphitic ribbons,” *Phys. Rev. B* **59**, 9858 (1999).
- ¹⁸J. Jung, T. Pereg-Barnea, and A. H. MacDonald, “Theory of interedge superexchange in zigzag edge magnetism,” *Phys. Rev. Lett.* **102**, 227205 (2009).
- ¹⁹A. R. Rocha, V. M. García-suárez, S. W. Bailey, C. J. Lambert, J. Ferrer, and S. Sanvito, “Towards molecular spintronics,” *Nat. Mater.* **4**, 335 (2005).
- ²⁰W. Han and R. K. Kawakami, “Spin relaxation in single-layer and bilayer graphene,” *Phys. Rev. Lett.* **107**, 047207 (2011).
- ²¹N. Tombros, C. Jozsa, M. Popinciuc, H. T. Jonkman, and B. J. van Wees, “Electronic spin transport and spin precession in single graphene layers at room temperature,” *Nature* **448**, 571 (2007).
- ²²L. R. F. Lima, A. R. Hernández, F. A. Pinheiro, and C. Lewenkopf, “A 50/50 electronic beam splitter in graphene nanoribbons as a building block for electron optics,” *J. Phys.: Condens. Matter* **28**, 505303 (2016).
- ²³P. Brandimarte, M. Englund, N. Papior, A. Garcia-Lekue, T. Frederiksen, and D. Sánchez-Portal, “A tunable electronic beam splitter realized with crossed graphene nanoribbons,” *J. Chem. Phys.* **146**, 092318 (2017).
- ²⁴S. Sanz, P. Brandimarte, G. Giedke, D. Sánchez-Portal, and T. Frederiksen, “Crossed graphene nanoribbons as beam splitters and mirrors for electron quantum optics,” *Phys. Rev. B* **102**, 035436 (2020).
- ²⁵S. Sanz, N. Papior, G. Giedke, D. Sánchez-Portal, M. Brandbyge, and T. Frederiksen, “Spin-polarizing electron beam splitter from crossed graphene nanoribbons,” *Phys. Rev. Lett.* **129**, 037701 (2022).
- ²⁶S. Sanz, N. Papior, G. Giedke, D. Sánchez-Portal, M. Brandbyge, and T. Frederiksen, “Mach-Zehnder-like interferometry with graphene nanoribbon networks,” *J. Phys.: Condens. Matter* **35**, 374001 (2023).
- ²⁷M. Koch, F. Ample, C. Joachim, and L. Grill, “Voltage-dependent conductance of a single graphene nanoribbon,” *Nat. Nanotechnol.* **7**, 713 (2012).
- ²⁸S. Kawai, A. Benassi, E. Gnecco, H. Söde, R. Pawlak, X. Feng, K. Müllen, D. Passerone, C. A. Pignedoli, P. Ruffieux, R. Fasel, and E. Meyer, “Superlubricity of graphene nanoribbons on gold surfaces,” *Science* **351**, 957 (2016).
- ²⁹L. Jiao, L. Zhang, L. Ding, J. Liu, and H. Dai, “Aligned graphene nanoribbons and crossbars from unzipped carbon nanotubes,” *Nano Res.* **3**, 387 (2010).
- ³⁰D. Wortmann, S. Heinze, P. Kurz, G. Bihlmayer, and S. Blügel, “Resolving complex atomic-scale spin structures by spin-polarized scanning tunneling microscopy,” *Phys. Rev. Lett.* **86**, 4132 (2001).
- ³¹J. Brede, N. Merino-Díez, A. Berdonces-Layunta, S. Sanz, A. Domínguez-Celorrío, J. Lobo-Checa, M. Vilas-Varela, D. Peña, T. Frederiksen, J. I. Pascual, D. G. de Oteyza, and D. Serrate, “Detecting the spin-polarization of edge states in graphene nanoribbons,” *Nat. Commun.* **14**, 6677 (2023).
- ³²A. Birtzclaff, A. Weismann, M. Brandbyge, and R. Berndt, “Shot noise as a probe of spin-polarized transport through single atoms,” *Phys. Rev. Lett.* **114**, 016602 (2015).
- ³³D. Wang, D.-L. Bao, Q. Zheng, C.-T. Wang, S. Wang, P. Fan, S. Mishra, L. Tao, Y. Xiao, L. Huang, X. Feng, K. Müllen, Y.-Y. Zhang, R. Fasel, P. Ruffieux, S. Du, and H.-J. Gao, “Twisted bilayer zigzag-graphene nanoribbon junctions with tunable edge states,” *Nat. Commun.* **14**, 1018 (2023).
- ³⁴L. S. Levitov, H. Lee, and G. B. Lesovik, “Electron counting statistics and coherent states of electric current,” *J. Math. Phys.* **37**, 4845 (1996).
- ³⁵D. A. Ivanov, H. W. Lee, and L. S. Levitov, “Coherent states of alternating current,” *Phys. Rev. B* **56**, 6839 (1997).
- ³⁶J. Keeling, I. Klich, and L. S. Levitov, “Minimal excitation states of electrons in one-dimensional wires,” *Phys. Rev. Lett.* **97**, 116403 (2006).
- ³⁷J. Dubois, T. Jullien, F. Portier, P. Roche, A. Cavanna, Y. Jin, W. Wegscheider, P. Rouleau, and D. C. Glatli, “Minimal-excitation states for electron quantum optics using levitons,” *Nature* **502**, 659 (2013).
- ³⁸A. Assouline, L. Pugliese, H. Chakraborti, S. Lee, L. Bernabeu, M. Jo, K. Watanabe, T. Taniguchi, D. C. Glatli, N. Kumada, H.-S. Sim, F. D. Parmentier, and P. Rouleau, “Emission and coherent control of levitons in graphene,” *Science* **382**, 1260 (2023).
- ³⁹J. Hubbard, “Electron correlations in narrow energy bands,” *Proc. R. Soc. A* **276**, 238 (1963).
- ⁴⁰J. C. Slater and G. F. Koster, “Simplified LCAO method for the periodic potential problem,” *Phys. Rev.* **94**, 1498 (1954).
- ⁴¹G. Trambly de Laissardière, D. Mayou, and L. Magaud, “Localization of Dirac electrons in rotated graphene bilayers,” *Nano Lett.* **10**, 804 (2010).
- ⁴²S. Sanz, N. Papior, M. Brandbyge, and T. Frederiksen (2022), Hubbard, v0.2.0
- ⁴³L. V. Keldysh, “Diagram technique for nonequilibrium processes,” *Sov. Phys. JETP* **20**, 1018 (1965).
- ⁴⁴L. Kadanoff and G. Baym, *Quantum Statistical Mechanics: Green’s Function Methods in Equilibrium and Nonequilibrium Problems, Frontiers in Physics: A Lecture Note and Reprint Series* (W. A. Benjamin, 1962).
- ⁴⁵M. Büttiker, Y. Imry, R. Landauer, and S. Pinhas, “Generalized many-channel conductance formula with application to small rings,” *Phys. Rev. B* **31**, 6207 (1985).
- ⁴⁶M. Büttiker, “Scattering theory of thermal and excess noise in open conductors,” *Phys. Rev. Lett.* **65**, 2901 (1990).
- ⁴⁷N. Papior, N. Lorente, T. Frederiksen, A. García, and M. Brandbyge, “Improvements on non-equilibrium and transport Green function techniques: The next-generation TRANSIESTA,” *Comput. Phys. Commun.* **212**, 8 (2017).
- ⁴⁸N. Papior (2021), SISL, v0.11.0, <https://doi.org/10.5281/zenodo.13745302>.
- ⁴⁹Y. Baskin and L. Meyer, “Lattice constants of graphite at low temperatures,” *Phys. Rev.* **100**, 544 (1955).
- ⁵⁰Y. X. Zhao and I. L. Spain, “X-ray diffraction data for graphite to 20 GPa,” *Phys. Rev. B* **40**, 993 (1989).

⁵¹B. Gaury and X. Waintal, “Dynamical control of interference using voltage pulses in the quantum regime,” *Nat. Commun.* **5**, 3844 (2014).

⁵²B. S. Popescu and A. Croy, “Efficient auxiliary-mode approach for time-dependent nanoelectronics,” *New J. Phys.* **18**, 093044 (2016).

⁵³A. Suresh, U. Bajpai, and B. K. Nikolić, “Magnon-driven chiral charge and spin pumping and electron–magnon scattering from time-dependent quantum transport combined with classical atomistic spin dynamics,” *Phys. Rev. B* **101**, 214412 (2020).